

## Chapter 7

### Electronic wave packets

#### 7.1 Introduction

Wave packet dynamics have been studied extensively on single electronic states (see previous chapters) and on multiple highly excited molecular Rydberg states[96]. Interactions between electronic states have also been observed in the context of observing unimolecular reactions such as dissociation[2, 4]. Yet the interactions between simultaneously propagating wave packets on intermediate energy electronic surfaces has received little attention[97-101]. Vast amounts of research have been undertaken to study interactions of electronic wave packets in atoms, but little has been addressed yet in molecules[102]. Calculations have addressed simple molecular systems such as  $H_2$ [97-99], and some experiments have been performed on the hyperfine splitting in molecular NO[101]. In all of these cases, the approximation can be made that the differences between interacting electronic states are small; all electronic states are approximately identical except for a total energy offset. Recently, experiments have been performed that control the angular momentum of electronic wave packets in atoms[103]. The primary reasons for this lack of study of electronic wave packets in molecules include the lack of efficient detection schemes or overall signal strength and lack of knowledge of the states[96]. In the case of  $Li_2$ , both of these conditions can be overcome. Much study has gone into the optimization of state resolved photoionization of  $Li_2$ , and significant excited state spectroscopy

has been performed, making the understanding of wave packets on highly excited electronic states possible[47, 104-110]. The experiments described in this chapter will examine an energetic region of  $\text{Li}_2$  that is at the upper end of those states that have proven theoretically tractable using standard spectroscopic experiments coupled with ab initio theory, while at the same time is at the lower end of those states whose description using “top down” techniques such as multichannel quantum defect theory is valid.

Using ultrafast pump-probe spectroscopy, we observe quantum beating between rovibrational states on the  $G^1\Pi_g^+$  and  $F^1\Sigma_g^+$  electronic curves of  $\text{Li}_2$ . Using a narrow bandwidth cw laser, a launch state is prepared on the  $A^1\Sigma_u^+$  electronic potential energy curve ( $v_A=11$ ,  $J_A=28$ ). From this launch state, a wave packet is prepared on these low lying Rydberg levels using the output from the OPA ( $\lambda_0 = 550 - 590$  nm) and is subsequently probed by a second near IR ultrafast pulse ( $\lambda_0 = 800$  nm). As the OPA wavelength is scanned, quantum beats between P, Q, and R branch rotational states for a progression of vibrational states on the G curve is observed. At a pump wavelength of 560 nm ( $G_e=35,000$   $\text{cm}^{-1}$ ,  $IP=41490$   $\text{cm}^{-1}$ ), in addition to rotational beating on the G curve ( $v_G=10-14$ ,  $J_G=27-29$ ), electronic beating between the G ( $v_G=13$ ,  $J_G=27-29$ ) and F ( $v_F=26$ ,  $J_F=27$ ) states is observed. As a result of the relatively low lying electronic states involved ( $n\sim 4$ ), there is a clear breakdown of the simplifying  $\Delta v=0$  propensity rule for quantum beating in high lying molecular Rydberg wave packet work[96, 102], indicating a complex vibrational structure.

The fact that the interfering states occupy different electronic states with different angular momenta suggests a potential handle for controlling dynamics. It has been shown in atoms that states with higher angular momentum are more sensitive to external fields than those with less angular momentum[111]. Through this mechanism, electric fields can be used to Stark shift one electronic state relative to the other[112]. This process has been exploited in designing molecular wave packets based upon the splitting of an electronic fine structure within a series of states with identical angular momentum[113].

This first part of this chapter will be divided into several sections, including a summary of the experimental techniques and a general overview of the energetic region being studied followed by presentation of the experimental results. Quantum beating between rotational states for a progression of vibrational levels on the  $G^1\Pi_g$  potential energy curve is shown as well as beating between states on the  $G$  and  $F^1\Sigma_g^+$  potential energy curve. An analysis and discussion of the experimental results including prospects for improvements in the experimental scheme will be posited. This chapter will then conclude with a summary of some experiments performed to understand a spurious transient signal observed with excitation by 670-690 nm light.

## 7.2 Experimental and Theoretical Overview

The experiments here focus primarily on the observation of wave packet dynamics in two excited electronic states that are accessible from launch state  $A^1\Sigma_u^+$ ,  $v_A, J_A=11,28$  ( $E_{tot}=17,151\text{ cm}^{-1}$ ). After preparation of this launch state, as

described in chapter 2, output from the OPA pumps accessible excited states, then ~800 nm ultrafast pulses photoionize those states pumped by the OPA output.

The central wavelength of the OPA output is scanned over a range from 17,000 to 18,000  $\text{cm}^{-1}$ , with a bandwidth of ~150  $\text{cm}^{-1}$  FWHM. The pump-probe delay is scanned over a range from about 0.0 ps to greater than 30 ps. In the weak field, parallel polarization, non-transient limit, the coherent signal can then be expressed as a variation of Eq. (1.1):

$$S(t) \propto \sum_f \sum_m |a_{fm}|^2 |a_{mi}|^2 + \sum_f \sum_m \sum_{n>m} |a_{fm} a_{mi} a_{fn} a_{ni}| \cos(\omega_{nm} + \phi_{nm,f}), \quad (7.1a)$$

where  $i$ ,  $f$ , and  $m$  ( $n$ ) refer to the launch, final, and intermediate states, respectively. All other terms have previously been defined, but an additional detail pertaining to the  $a_n$  coefficients will be helpful:

$$a_{21} \propto \varepsilon(\omega_{21}) \langle v_2 J_2 | \hat{\mu}_{elec}(R) | v_1 J_1 \rangle, \quad (7.1b)$$

where 2 and 1 refer to the final and initial states of a particular single photon transition. Note that the transition dipole moment operator  $\hat{\mu}_{elec}(R)$  is now dependent on both the specific pair of states in a transition and the vibrational coordinate  $R$ [105]. The implications of this are twofold: the transition dipole moment operator may lead to an element that can be controlled, and the FCF is more complex than a simple vibrational overlap[105].

Several bound electronic states are energetically accessible from the launch state with a pump pulse energy of 17,800  $\text{cm}^{-1}$ [104, 107-110]. See Fig. 7.1 for the potential energy surfaces in the region examined here. Five singlet electronic states are bound with a total energy around 35,900  $\text{cm}^{-1}$  total energy.

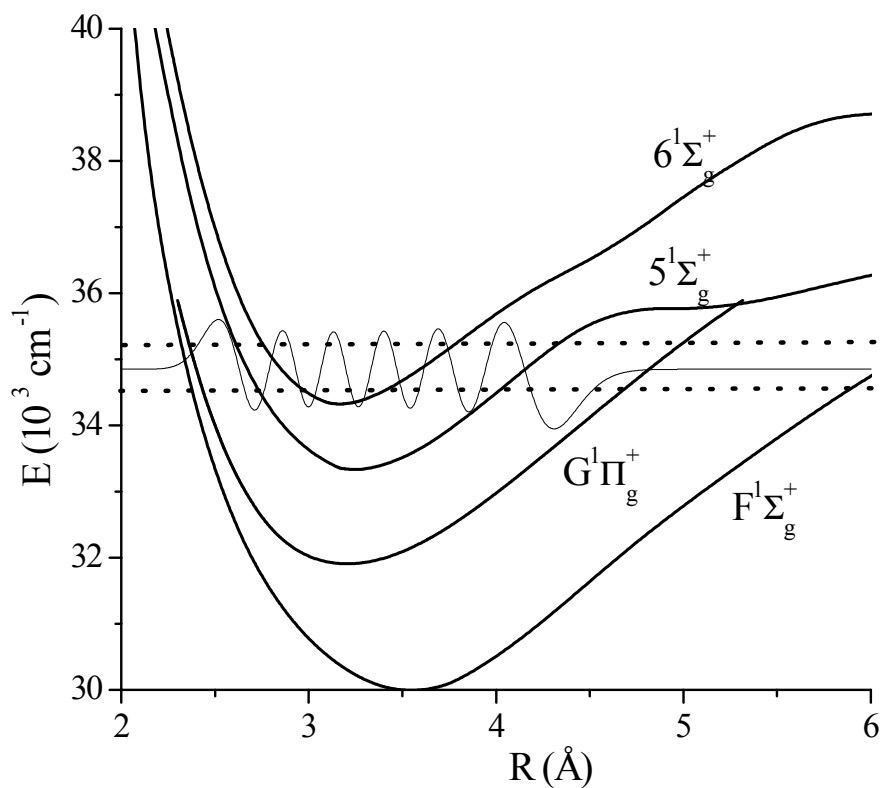


Figure 7.1: Potential energy curves in excitation region. Also shown is the launch state wavefunction superimposed on the relevant energy regions, as bounded by the horizontal dotted lines. The F, G, and 5 & 6 curves are taken from references [104], [109], and [108], respectively. At the relevant energies here, the low lying  $E^1\Sigma_g^+$  state is bound by less than  $500\text{ cm}^{-1}$ , so it is not included in the figure.

displaying the discrete wave packet dynamics that will be examined later. The  $E^1\Sigma_g^+$  state is bound, but is very near its dissociation limit ( $35,700\text{ cm}^{-1}$ ) in the experiments examined here, and its near continuum behavior precludes it from  $5^1\Sigma_g^+$  and  $6^1\Sigma_g^+$  states are included in the figure, but with the  $v=11$  launch state, the low lying vibrational levels that are accessible have small vibrational overlap with this launch state wavefunction. The inner and outer turning points of the  $5^1\Sigma_g^+$  and  $6^1\Sigma_g^+$  states fall within the spatial extent of the launch state wave function that is completely oscillatory. In contrast, the inner walls of the F and G potentials nearly touch, and overlap well with the inner part of the launch state wave function. In fact, calculations predict three orders of magnitude smaller vibrational overlap between the launch state and accessible states on the 5 and 6 states compared to accessible levels on the F and G states. This analysis is only a first approximation, neglecting overlap with the vibrational wavefunction of the final, autoionizing Rydberg state. Also, small deviations in the functional form of the transition dipole operator with respect to R can introduce uncertainties to the simple calculation referred to above, but for the large differences in vibrational overlap such as this, the above conclusions remain qualitatively valid.

Working from the assumption that only the F and G states play a role in the dynamics seen here, a portion of the spectrum of states that can be excited via strongly allowed transitions from the launch state is shown in Fig. 7.2. The F and G states are based upon fits to experimental data and are calculated according to the following expression[109, 110]:

$$E_{tot} = G_v + B_v[J(J+1)-1] - D[J(J+1)-1]^2 + q[J(J+1)] \quad (7.2)$$

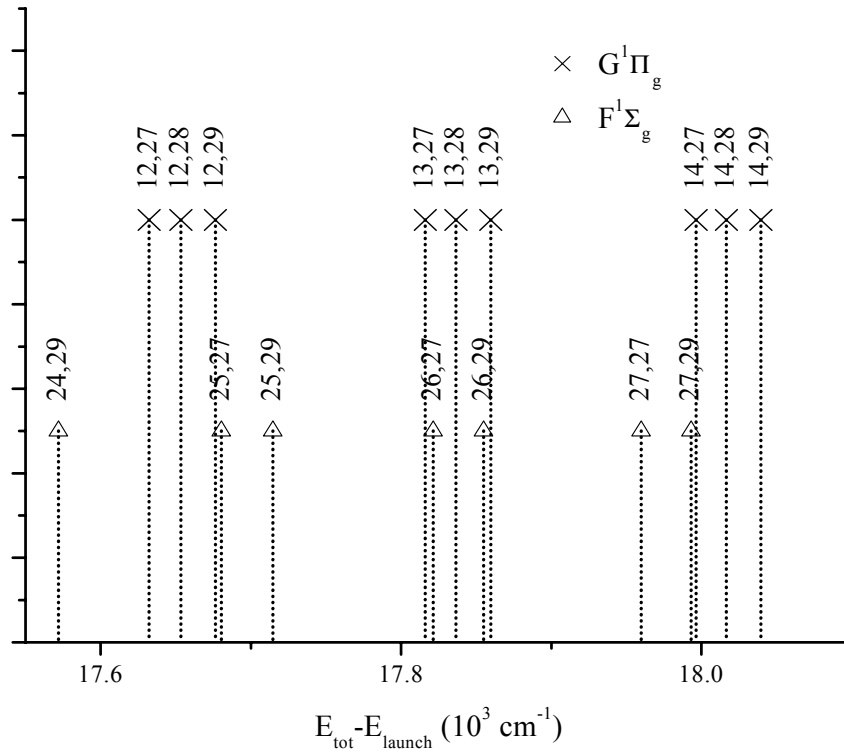


Figure 7.2: State locations accessible from the  $v_A, J_A=11, 28$  launch state with a central pump energy of  $17,550 \text{ cm}^{-1}$  to  $18,100 \text{ cm}^{-1}$ . P and R branch transitions are included for the  $F^1 \Sigma_g^+$  state, and P, Q, and R branches are included for the  $G^1 \Pi_g^+$  state. States are labeled as (v, J).

where  $G_v$  is the energy for vibrational level  $v$ ,  $B_v$  is the rotational constant for vibrational level  $v$ ,  $D$  is the centrifugal distortion constant, and  $q$  is the  $\Lambda$  doubling parameter. The centrifugal distortion constants are calculated based upon the Dunham fit parameters for the rotational constant  $Y_{01}$  and vibrational frequency  $Y_{10}$  so that  $D=4Y_{01}^3/Y_{10}^2$ [114]—approximately  $4.31 \times 10^{-6} \text{ cm}^{-1}$  and  $7.84 \times 10^{-6} \text{ cm}^{-1}$  for the F and G states, respectively. The  $\Lambda$  doubling parameter only applies to vibrational levels on the G state, splitting each rotational level into two, hence the term “doubling” parameter. For even  $J_G$ , the higher lying state has (+) parity, and the lower lying state has (-) parity, and for odd  $J_G$ , this is reversed. To maintain the  $+\leftrightarrow-$  parity selection rule, this means that the P and R transitions excite the higher level, and the Q branch the lower level, of each  $J_G$  doublet[112]. This means that in Eq. (7.2), the  $\Lambda$  doubling parameter only applies to the P and R branches of the G state. All constants for the F state are taken from refs. [107, 115], except for the centrifugal distortion constant which is taken from ref. [116].  $V$ ,  $B$ , and  $q$  for  $v_G=11$  and 12 are taken from ref. [109], and the rest of the constants for the G state are taken from ref. [110]. The state energies for the F state around  $v_F$ ,  $J_F=26, 27 \& 29$  have not been experimentally determined elsewhere, so the fit values have been given with an error of  $0.25 \text{ cm}^{-1}$  assumed. In the G state, similar errors should be assumed.

### 7.3 Results

As stated previously, the observed wave packets show very slowly decaying behavior, as shown in Fig. 7.3. Figure 7.3a shows the time domain pump-probe signal using a pump pulse with a central energy of  $17,850 \text{ cm}^{-1}$ , and a

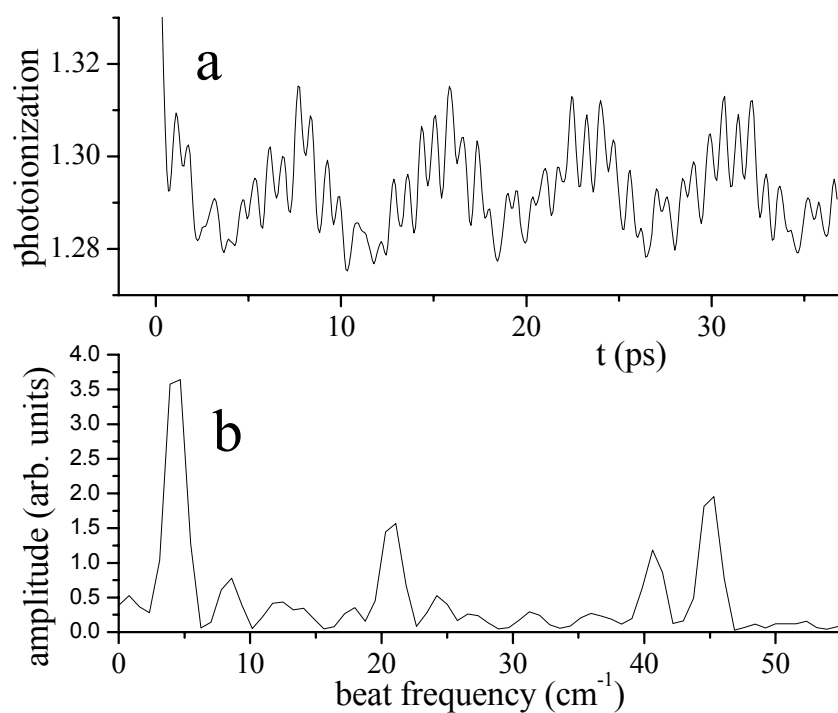


Figure 7.3: Pump-probe signal for a pump energy of  $17,850 \text{ cm}^{-1}$  for a launch state of  $v_A, J_A=11,28$ . Panel a shows the photoionization signal as a function of pump-probe delay. Panel b shows the Fourier Transform of the signal from panel a. Beats at energies of  $4, 21, 41,$  and  $45 \text{ cm}^{-1}$  are clearly present. Possible peaks are also located at  $8 \text{ cm}^{-1}$  and  $25 \text{ cm}^{-1}$ .

bandwidth of  $150 \text{ cm}^{-1}$  FWHM. Notice that there is a very pronounced low frequency oscillation present along with several higher frequency oscillations. To analyze the nature of the beats, an FT is performed on the signal after  $t=0.0 \text{ ps}$ . The Fourier Transform of this signal shows four pronounced peaks in the beat spectrum. Beats are observed at approximately  $4, 21, 41,$  and  $45 \text{ cm}^{-1}$ . Each of these peaks is very narrow, in fact their width is defined by the pump-probe scan length. This narrow linewidth suggests that the interfering wavefunctions are relatively stable and do not quickly decay to secondary states.

To identify the quantum beats in Fig. 7.3, the pump pulse energy was varied in an attempt to view any spectral trends. Figure 7.4 shows the FT spectra of the quantum beats observed for a variety of central pump energies ranging from  $17,100 \text{ cm}^{-1}$  to  $18,200 \text{ cm}^{-1}$ . In the figure, each spectrum has been offset on the vertical axis to show the relative pump pulse energy. The spectral amplitudes have been normalized so that the beats around  $45 \text{ cm}^{-1}$  have similar amplitudes. In the case where no beats were observable above the noise level, the spectra were normalized so that the strongest peak in the spectrum coincides with the amplitude of the observable beats around  $45 \text{ cm}^{-1}$  [see spectra at  $17,500 \text{ cm}^{-1}$  and  $17,600 \text{ cm}^{-1}$ ]. Due to large instabilities in the experimental apparatus, the amplitudes of the beats are generally unreliable, so an analysis of the spectral amplitudes is generally intractable. However, the *frequencies* of the quantum beats can be reliably observed since, in the weak field limit, the frequencies are independent of the laser intensity or overlap and only need to be sufficiently above the noise to detect [see Eq. (7.1a)]. Each of the peaks that have amplitude

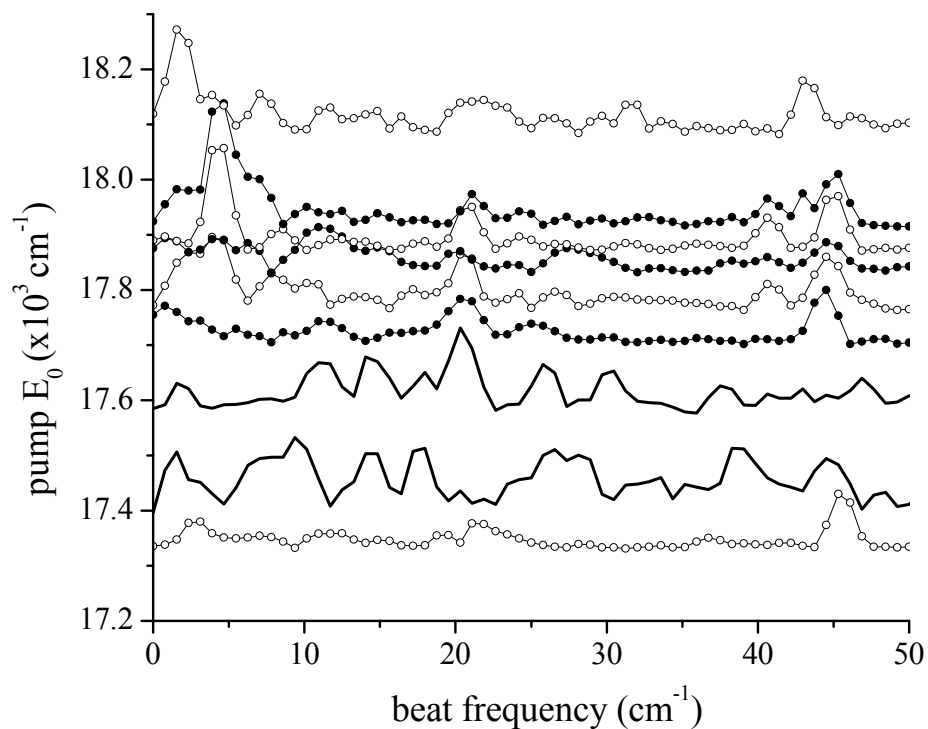


Figure 7.4: Fourier Transform quantum beat spectra for varying pump energies. All traces have been rescaled to show peaks at around  $45 \text{ cm}^{-1}$ , if present. Where no significant peaks are visible (solid lines), the spectra have been amplified to show the noise baseline. All spectra have been offset to reflect their respective pump pulse energy. Where peaks are clearly above the noise level, the frequency is recorded.

more than twice the noise level were fit with a Gaussian lineshape, and the central frequency is obtained.

A summary of the observed beats as a function of central pump energy is plotted in Fig. 7.5. The error bars for the beat frequencies reflect the widths of the peaks as recorded in Fig. 7.4, except the lowest frequencies which have a higher error due to laser drift as a function of delay stage position. Also included in the figure are the predicted beat frequencies assuming rotational quantum beating in the  $G^1\Pi_g^+$  state, and where they are expected to be at their respective maxima. Several trends in the quantum beat frequencies should be noted. First, the beat around  $45\text{ cm}^{-1}$  shows a trend toward lower frequencies as the pump energy is increased. The beat around  $21\text{ cm}^{-1}$  shows similar behavior, although the degree of change falls within the error bars of the quantum beats. Around pump energies of  $17,700\text{ cm}^{-1}$  to  $18,100\text{ cm}^{-1}$ , additional beats around  $2, 4, 25,$  and  $41\text{ cm}^{-1}$  are observed. These beats are clearly not a part of the overall progression, lending credence to the possibility that the beats are something other than simple rotational beats in the G state. Also included in the figure is a schematic spectrum with a central wavelength of  $17,880\text{ cm}^{-1}$  and a FWHM bandwidth of  $200\text{ cm}^{-1}$ . This illustrates that quantum beats can be present even if the central pump pulse energy is shifted from the location of the peak beat amplitude. Given that the quantum beats have energies around  $45\text{ cm}^{-1}$ , it is concluded that the predominant state at play in this case is the  $\Delta J=2$  rotational beat in the  $G^1\Pi_g^+$  state. This fits well with previous cw type spectroscopy since the  $\Delta J=2$  rotational spacing in the  $F^1\Sigma_g^+$  and  $5^1\Sigma_g^+$  states are  $34\text{ cm}^{-1}$  and  $52\text{ cm}^{-1}$ , respectively. Additionally, the

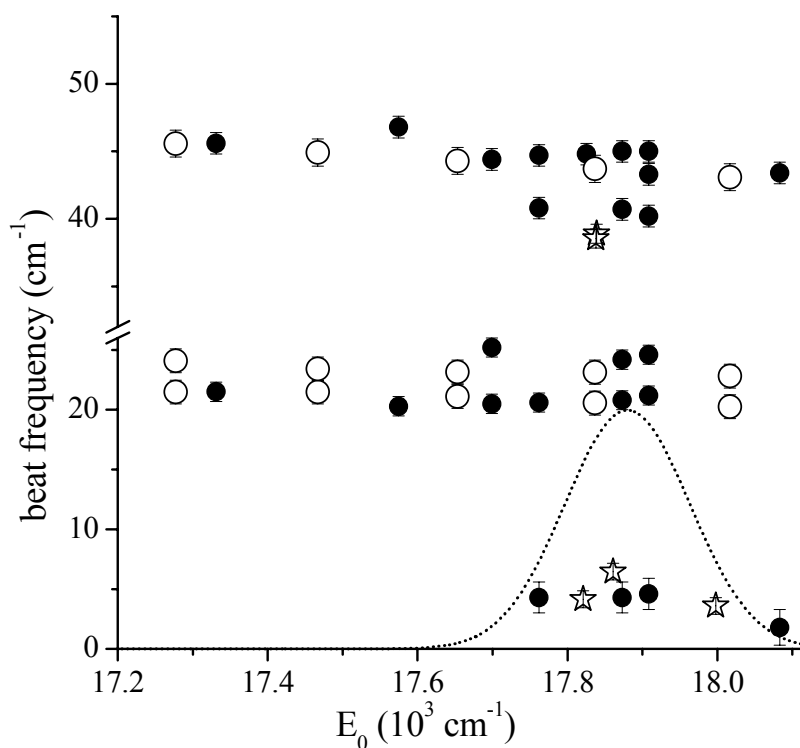


Figure 7.5: Quantum beat energy as a function of central pump pulse energy for 11,28 launch state. A sample spectrum with central energy of  $17,880 \text{ cm}^{-1}$  is included as a measure of pump pulse bandwidth. Closed circles are experimental quantum beat frequencies for different pump energies. Open circles are predicted rotational quantum beats in the G state, and stars are predicted beat frequencies between the F and G states around  $17,850 \text{ cm}^{-1}$  and  $18,000 \text{ cm}^{-1}$  as tabulated in Table 7.1.

progression of rotational beats around  $21 \text{ cm}^{-1}$  fit well with a  $\Delta J=1$  beat ( $J_G=27&28$ ) that is only possible in the G state due to the  $\Delta\Lambda=1$  electronic component of the transition from A  $^1\Sigma_u^+$  state. It is interesting to note that the  $J_G=28&29$  beat around  $23 \text{ cm}^{-1}$  is predominantly absent from these spectra. Since this beat is observed with a rather weak amplitude in several of the traces, the predominant absence of these higher frequency  $\Delta J=1$  beats is attributed to a systematically weak transition dipole moment to the Q-branch  $J_G=28$  state as well as a preferential excitation to  $J_G=27$  over  $J_G=29$ . Even though the observed quantum beat amplitudes involving the Q-branch states are less than predicted by Hönl-London factors, the line positions coincide with the expected positions[92].

To further verify that the main progressions seen are indeed rotational beats in the G state, a similar series of experiments was carried out for a different launch state. To make sure that any effects related to FCFs are minimized, the same vibrational launch state is chosen but the J state is changed, so that  $v_A, J_A=9, 16$ . Assuming the main progression is due to pairs of rotational states ( $J_G=15&17$ ), the progression should be reproduced. Due to different rotational constants for the F and G potentials, a change in J would result in a shift of the states on one potential relative to the other. Figure 7.6 shows that the vibrational progression of rotational beats is reproduced, with no other beats present, failing to disprove the “extra” beats of Fig. 7.5 are beats between electronic states. Again in this lower J case, the rotational quantum beats involving the Q branch are weaker than those between the P and R branch states and only show the lower frequency beat, except for one low amplitude  $14 \text{ cm}^{-1}$  beat at  $E_0=17,530 \text{ cm}^{-1}$ .

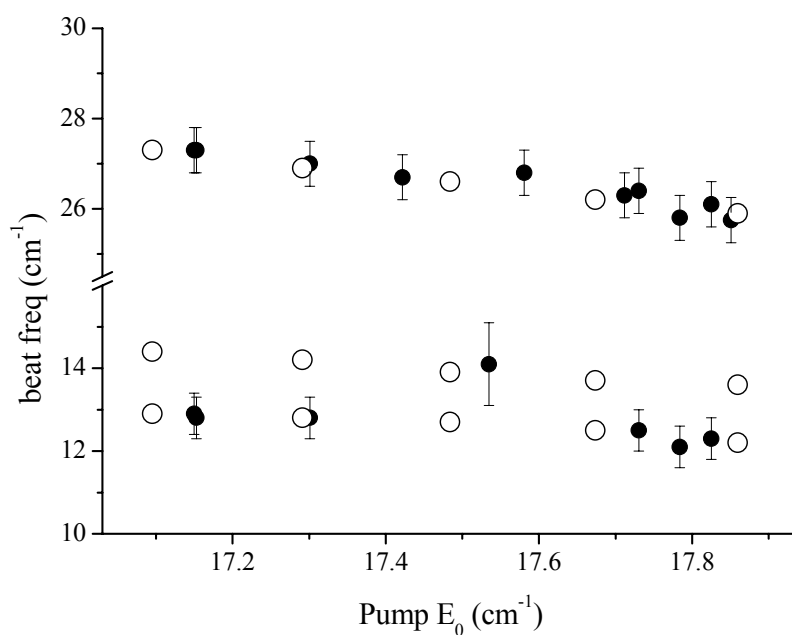


Figure 7.6: Quantum beat frequencies as a function of central pump energy from 11,16 launch state. Closed circles are experiment, and open circles are predicted rotational beats for different vibrational levels of the G state. The beat at  $E_0=17,530 \text{ cm}^{-1}$  has large error bars because its presence was determined in the presence of significant noise.

The absence of additional beats in this progression is attributed to a shift in the F state energy levels due to different rotational constants for the F versus the G states. This further verifies that the beats are in fact rotational and not vibrational in nature. If the additional beats seen for the 11, 28 launch state were confined to the G state, they would be observed from this second launch state, but they are not.

#### 7.4 Discussion and Future Directions

Previously completed high resolution spectroscopy suggests the wave packet excited with  $17,850\text{ cm}^{-1}$  contains contributions from both the G and F states, although the reported state to state energy fits deviate up to  $0.3\text{ cm}^{-1}$ , depending upon the source[107, 109, 110, 115, 116]. Since the  $G\leftarrow A$  transition consists of  $\Delta\Lambda=1$ , single photon selection rules allow  $\Delta J=0, \pm 1$  transitions, hence the presence of the P, Q, and R branch states. The  $F\leftarrow A$  transition corresponds to  $\Delta\Lambda=0$ , so parity selection rules allow  $\Delta J=\pm 1$ , so only the P and R branch states of the F state are excited. Again, here only the line positions are shown; information regarding transition strength is not included. To identify quantum beats, energy differences must be taken into account, and these values have been summarized in Table 7.1.

Upon examining the expected quantum beat frequencies, the participating states can be inferred. Around  $17,850\text{ cm}^{-1}$ , the P-R beat in the G state [*i.e.*  $G(13,27)-G(13,29)$ ] is seen as the  $45.0\text{ cm}^{-1}$  beat, as was established before. The P-Q beats are near their expected values at slightly less than half the P-R

**$E_{pu}=17,850\text{cm}^{-1}$**

		State (v, J)			
		F(26,27)	G(13,28)	F(26,29)	G(13,29)
State (v, J)	$E_{\text{tot}} - E_{\text{launch}}/$	17821.3	17836.6	17854.9	17859.7
G(13,27)	17816.0	(5.3)	20.6	38.9	43.7
F(26,27)	17821.3		(15.3)	(33.6)	(38.4)
G(13,28)	17836.6			18.3	23.1
F(26,29)	17854.9				4.8

**$E_{pu}=18,000\text{cm}^{-1}$**

		State (v, J)			
		F(27,29)	G(14,27)	G(14,28)	G(14,29)
State (v, J)	$E_{\text{tot}} - E_{\text{launch}}/$	17993.0	17996.3	18016.5	18039.4
F(27,27)	17959.9	(33.1)	(36.4)	(56.7)	(79.5)
F(27,29)	17993.0		3.3	(23.5)	(46.4)
G(14,27)	17996.3			(20.3)	43.1
G(14,28)	18016.5				(22.8)

Table 7.1: Expected quantum beat frequencies. For pump pulses centered around  $17,850\text{ cm}^{-1}$  and  $18,000\text{ cm}^{-1}$ , optically allowed rovibrational states on the F and G electronic curves are listed, along with their total energies. The quantum beat frequency is the difference in energies. Unobserved quantum beats are in parentheses.

frequency due to the  $\Lambda$  doubled spectrum of the G state. Interestingly, when they are observed, the Q-R beats are very weak and have a frequency over  $1.0 \text{ cm}^{-1}$  away from the predicted frequency. Almost all of the beats involving the F(26, 27) state are observed, with the beats at  $4.2 \text{ cm}^{-1}$  and  $40.9 \text{ cm}^{-1}$  observed. The absence of beats involving state F(26, 29) indicate that the photoionization pathway for that state is weak. Calculations show the vibrational overlap between the F(26, 29) and the ion ground state  $X^+(25, 28)$  is very near zero. At the energies observed here, ionization proceeds through the  $X^+(24, 28)$  state which has nonzero vibrational overlap with F(26, 29), but it should be remembered that there is a small difference in the meanings of the vibrational contribution to a transition dipole and the vibrational overlap between states:  $\hat{\mu}_{elec}(R)$ . Vibrational overlap calculations assume that  $\hat{\mu}_{elec}(R)$  is constant over all R, but even at the small R where there is appreciable vibrational wavefunction in the states observed here, there will be small variations in the transition dipole operator. This means that the vibrational overlap calculations provide qualitative information, but fail to quantitatively characterize the transition strength.

Future experiments can be undertaken that can improve or exploit the effects seen here. In these experiments, quantum beat frequencies are observed as the pump wavelength is tuned. Since the probe light is the 800 nm fundamental from the regenerative amplifier, the final energy of the system is tuned along with the intermediate energy. In order to reduce the number of degrees of freedom in the analysis of the data, it would be advantageous to keep the final energy fixed. This could be overcome somewhat by simultaneously tuning the regenerative

amplifier output along with the OPA wavelength. This will technique will be limited since the optimization of the OPA output depends a great deal on the input pulse characteristics. An alternate means to keep the final energy fixed would be to include the addition of either a second OPA or the use of a second order of output from the OPA in these experiments. Since the signals are still rather weak at this point, the addition of a second OPA is possibly not feasible due to losses in the production of OPA light.

In this series of experiments, we have shown progressions of P-R, Q-R, and Q-P rotational quantum beats on various vibrational levels of the  $G^1\Pi_g^+$  state of  $Li_2$ . In addition to these single electronic surface quantum beats, we have observed and identified various quantum beats between states on the G state and the  $F^1\Sigma_g^+$  state. This observation of low lying Rydberg wave packets begins to bridge the gap between relatively low energy, hence isolated, wave packets on single electronic curves and high lying, nearly ionic Rydberg levels. Additionally, this work sets a benchmark for the types of signals to be expected as the total energy of a system increases towards the ionization limit.

## **7.5 Ultrafast transient behavior with 680 nm excitation**

In the previous sections of this chapter, a type of electronic interaction was examined, where bound wave functions on separate electronic states beat against each other. In an effort to identify as many regions with observable wave packet dynamics such as in the previous section, we scanned other wavelength ranges.

In the process, another interesting spectroscopic feature was found: we observe a very large, transient, photoionization (PI) signal for a pump energy around 14,700  $\text{cm}^{-1}$  while exciting the  $v_A, J_A=11,28$  launch state. In fact, we see up to 100 times the total PI signal at short times relative to longer times, as shown in Fig. 7.7.

Since this effect is so strong, it is studied to try to identify potentially useful traits. Much of the data support the conclusion that the fast decaying signal is an atomic ionization, motivating us to preempt further study of this effect with several of the studies presented in chapters 5 and 6.

The following section will begin with an examination of the spectral extent of the large transient peak. To verify that the transient effect is not a result of an isolated predissociative rovibrational state, launch states with  $J_A=16, 28,$  and 40 are compared. Next, the dependence of the transient signal on the pump polarization is presented. Finally, the results are discussed, and a very simple atomic mechanism will be proposed to explain the ultrafast effect. A significant unanswered question regarding the observed decay time is also presented.

### 7.5.1 Experiment and Results

The experimental setup for this section is nearly identical to that in the previous section, except that the wavelength range scanned by the OPA is slightly longer. In the experiments described here, a central wavelength range of approximately 650-700 nm (14000-15400  $\text{cm}^{-1}$ ) will be examined. Generally, the pump bandwidth is about 200  $\text{cm}^{-1}$  FWHM. Since the wavelengths studied here are at the edge of the spectral output from the OPA, the bandwidth can be greatly

expanded due to nonidealities in the OPA alignment, further limiting the reliability of the spectral studies in this section. In all discussions, the central

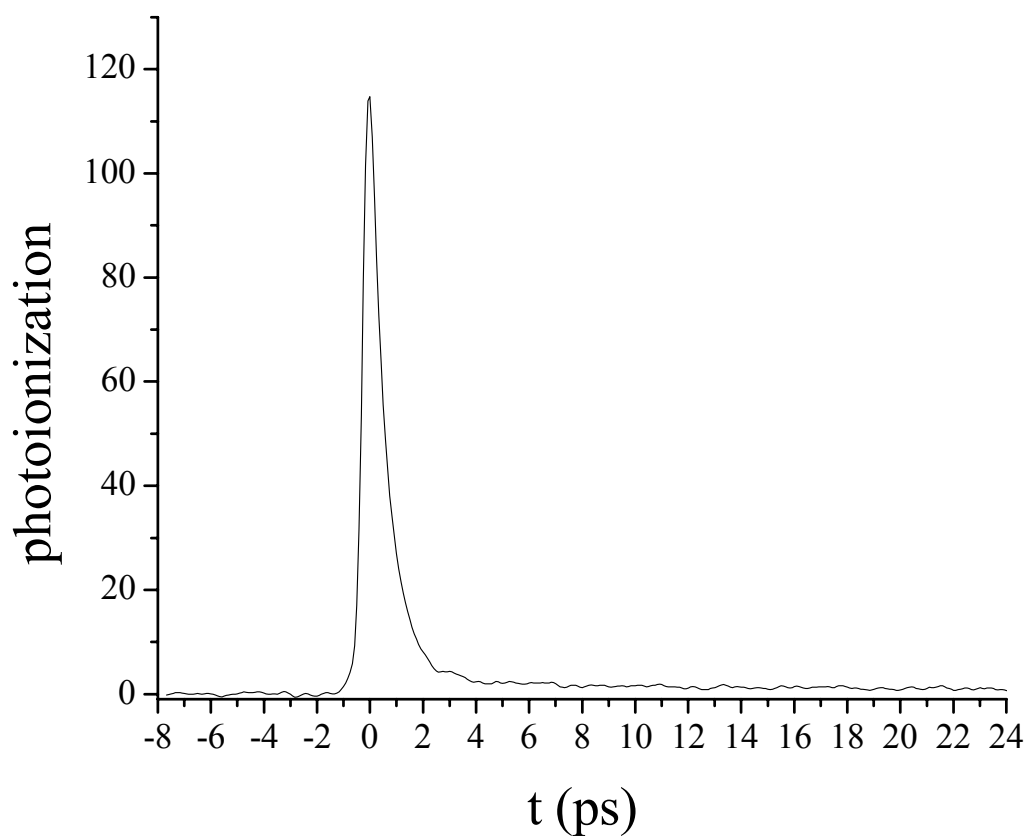


Figure 7.7: Pump-probe signal for  $E_{pu}=14,700 \text{ cm}^{-1}$ . Probe polarization is parallel, and the photoionization (PI) has been normalized so that  $PI=0$  for  $t<-4.0$  ps, and  $PI=1$  for  $t>20$  ps.

energy of the approximately Gaussian spectral envelope will be cited as  $E_{\text{pu}}$ . Typical OPA output power is approximately 60 mW, but the power at the heat pipe is considerably less ( $\sim 20$  mW) due to losses along the optical path.

To test whether the transient peak was unique to a specific cw frequency, launch states with  $\nu_A=11$  and  $J_A=16, 28,$  and  $40$  are excited with cw light at 603, 606.955, and 613. nm, respectively. Figure 7.8 shows the transient peak amplitudes for  $E_{\text{pu}}$  for  $J_A=16, 28,$  and  $40$ . From all launch states, pump-probe transients show a similar transient behavior with a quickly decaying peak followed by a stable incoherent photoionization signal. Obviously, from this figure, there is no reliable  $J_A$  dependence to the transient signal. The spectral profile of the  $J_A=28$  data shows a small ( $\sim 100$   $\text{cm}^{-1}$ ) shift relative to  $J_A=16$  and  $40$ , but there is still significant overlap of the profiles.

Finally, the pump polarization was rotated relative to the cw and probe pulses from parallel to the magic angle and perpendicular. Figure 7.9 shows a semilog plot of the pump-probe traces at each of these three critical polarizations for  $E_{\text{pu}}=14700$   $\text{cm}^{-1}$ , giving unexpected results. In the Fig. 7.9a, the traces have been normalized so that the signal for  $t<4.0$  ps is set to zero, and the signal for  $t>10$  ps is set to 1. Clearly, the transient signal goes down relative to the long time signal. The traces are characterized by an initial exponential rise time where  $t_{1/2}=0.16$  ps, as should be expected from the timescale of the pump pulse. After  $t=0.0$  ps, all of the traces exhibit exponential decay behavior with halflives of between 0.43 and 0.59 ps. The parallel and perpendicular signals both show slower ( $t_{1/2}\sim 8$  ps) decays, but with much lower amplitude, making quantitative

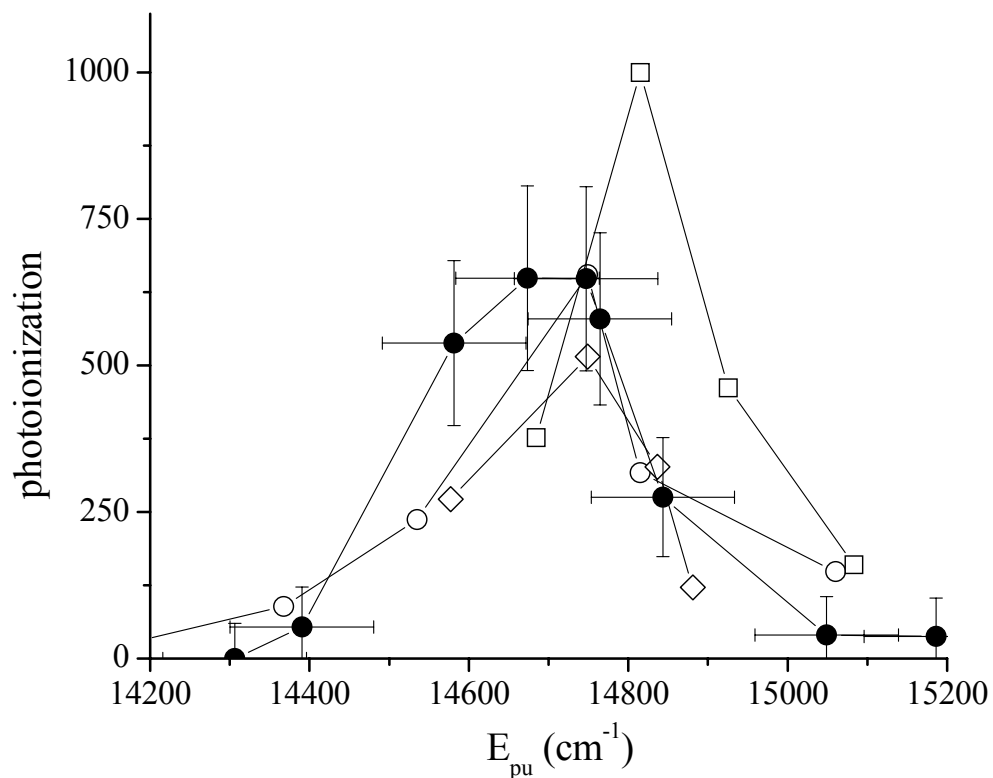


Figure 7.8: Dependence of transient peak height on central pump energy and  $J_A$ . The peak photoionization is been plotted as a function of central pump energy for  $J_A=16$  ( $\diamond$ ),  $J_A=28$  ( $\circ, \bullet$ ), and  $J_A=40$  ( $\square$ ). In all cases  $v_A=11$ . The solid circle dataset was taken before a lab relocation, and the open symbols were taken after; this is given to show the repeatability of the data. The error bars given for one data set are similar for the others.

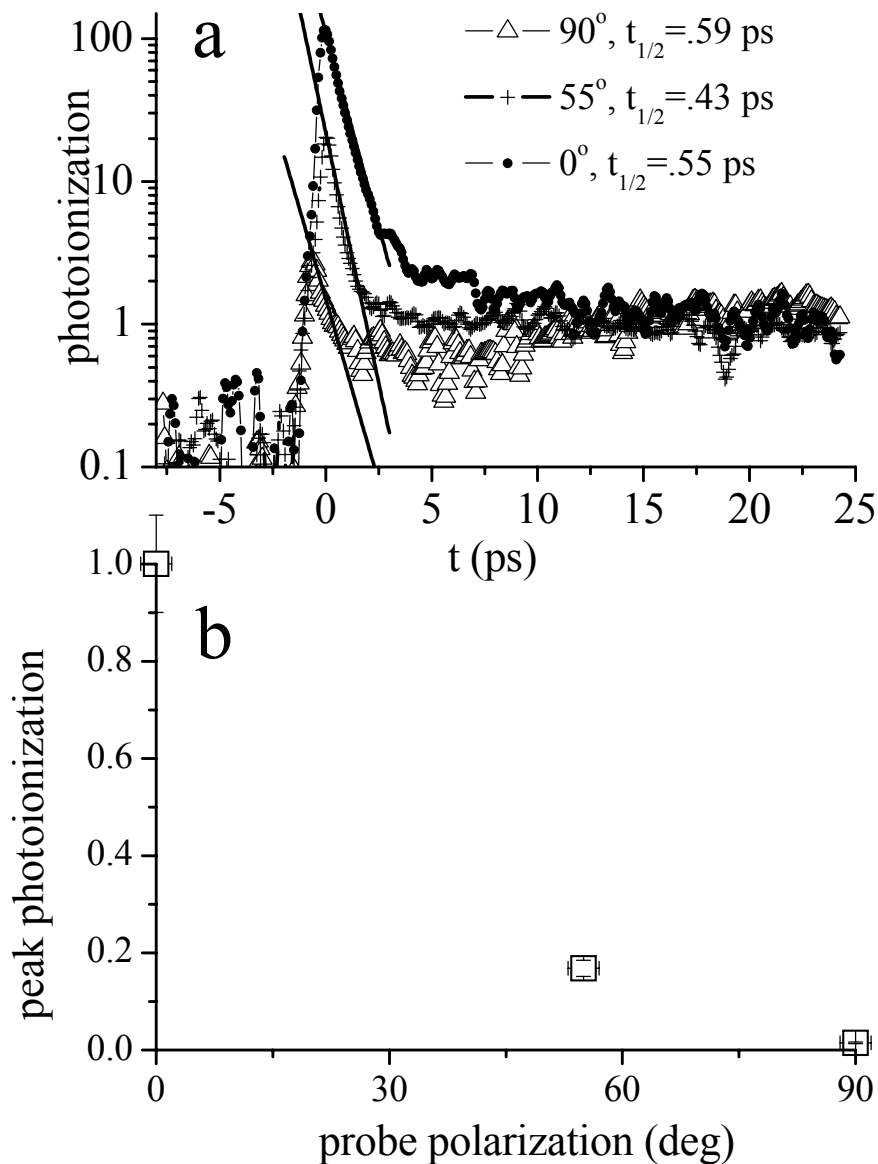


Figure 7.9: Polarization dependence of peak photoionization for parallel, perpendicular, and magic angle pumps. Panel a: Pump-probe traces for each probe polarization. The solid lines are single exponential decay fits, with half-lives ranging from 0.43 to 0.59 ps. Panel b: Peak photoionization (relative to  $t > 20$  ps) as a function of pump polarization.

conclusions difficult. Figure 7.9b shows the peak amplitude as a function of probe polarization. It is clear that there is a dramatic decrease in the transient signal as a function of degrees off parallel.

### 7.5.2 Discussion

The data suggest that the main transient peak is an atomic, not molecular, effect. The predominant transient time dependent effect appears to come from an excitation to the quickly decaying  $2p \rightarrow 2s$  atomic transition, resulting in a 1+3 photoionization pathway. To ionize, a total energy of  $43,300 \text{ cm}^{-1}$  is needed. This means that the  $2p$  electron needs an additional  $28,400 \text{ cm}^{-1}$ , so a three photon resonance enhanced photoionization pathway with the  $800 \text{ nm}$  probe is suggested. The resonant enhancement may be possible since the energy between the  $2p$  and  $3p$  electronic levels is only  $13,000 \text{ cm}^{-1}$ , very near the probe energy, and to reach the ion an additional  $15,900 \text{ cm}^{-1}$  are needed. Three primary pieces of evidence support this atomic photoionization pathway conclusion: the polarization dependence of the signal, the fluorescence linewidth for the  $2p \rightarrow 2s$  transition, and the similarities of the transient signal with and without the cw laser present. The observed lifetime of the transient peak is three orders of magnitude shorter than the literature value for spontaneous decay for the suggested transition; this large deviation from literature values requires further study before making a definitive conclusion for the transient effect seen.

That the main transient effect is atomic in nature is supported by the dependence of the photoionization on the polarization of the pump and probe

pulses. As it was shown in Fig. 7.9, the transient signal is nearly completely depleted by a simple rotation of the pump polarization relative to the probe. In a molecular system, this should not necessarily be the case. Assuming that there is a non-uniform  $m_j$  distribution in the state prepared by the probe (i.e. the state is aligned), the perpendicular signal should not go to zero. By setting the probe polarization to perpendicular relative to the probe, or rotating the frame of reference by  $90^\circ$ , the effect (disregarding coherences) is approximately a swap of the effective  $m_j$  assignments from high to low and vice versa. We can quantify the alignment dependent contribution to the signal, assuming a uniform  $m_j$  distribution in the launch state, as the following:

$$S_{align} = \left| \sum_{pu=-J}^J \langle M_{prf} | \hat{\mu}_{pr} | M_{pri} \rangle \langle M_{puf} | \hat{\mu}_{pu} | M_{pui} \rangle \right|^2, \quad (7.3)$$

where  $M$  is the aligned spherical harmonic wavefunction with a specific  $J$ ,  $i$  and  $f$  refer to the initial and final states of a transition, and  $pu$  and  $pr$  refer to the pump and probe steps. Here, it is assumed that all transitions follow the selection rule  $\Delta m_j=0$ . In the parallel case, the  $m_j$  quantum numbers  $pu=pr$ . For the perpendicular case, the quantum numbers can be approximated by  $|pr| \approx J - |pu|$ , so that in effect, the  $m_{J_{pu}}=0 \rightarrow m_{J_{pr}}=\pm(J-1)$  and  $m_{J_{pu}}=\pm(J-1) \rightarrow m_{J_{pr}}=\pm 1$ . The effect of this transformation is that for  $J=27$ , the signal decreases by at most 13%. In  $\text{Li}_2$ , only the electronic ground state of the ion, which is known to have sigma symmetry, is reachable with a single photon from each of the pump and probe pulses. This requires that both pump and probe dipole moment operators lie along the same axis relative to the molecular axis, further justifying the analysis above.

This is all in contrast to the atomic case, where it is well known that a 1+3 photon absorption by an electron shows  $\cos^2(\theta)$  dependence where  $\theta$  is the angle between photon polarizations. This is the first bit of evidence that the transient effect seen in Fig. 7.7 is an atomic effect.

In the dispersed fluorescence spectrum under excitation by the 606.955 nm cw laser, many doublet lines appear that correspond to P and R branch decays from the launch state, as well as regularly spaced collisionally induced satellite lines. An additional line appears that is not part of these progressions at 670.5 nm. Figure 7.10 shows a portion of the dispersed fluorescence spectrum with a doublet at 14,770 and 14,830  $\text{cm}^{-1}$  along with an additional prominent line at 14,910  $\text{cm}^{-1}$ . The line at 14,910  $\text{cm}^{-1}$  corresponds to the exact expected wavelength of the 2p $\rightarrow$ 2s atomic transition, and in fact appears in the dispersed fluorescence spectra for many different excitation wavelengths. Higher resolution spectra even show the spin orbit splitting of less than 0.3  $\text{cm}^{-1}$  for the 2p state. The linewidth is clearly wider than the molecular lines (the molecular linewidth here is primarily determined by the instrument response). The observation of a broadened line in the dispersed fluorescence spectrum only suggests a short lifetime. Since the linewidth is so much greater than expected from tabulated lifetimes, a significant problem exists with concluding a mechanism based upon this evidence.

One final piece of evidence supports the argument that the observed effect is a result of an atomic, not molecular process. The pump-probe traces observed above were gathered using a three beam interaction, but they can also be seen

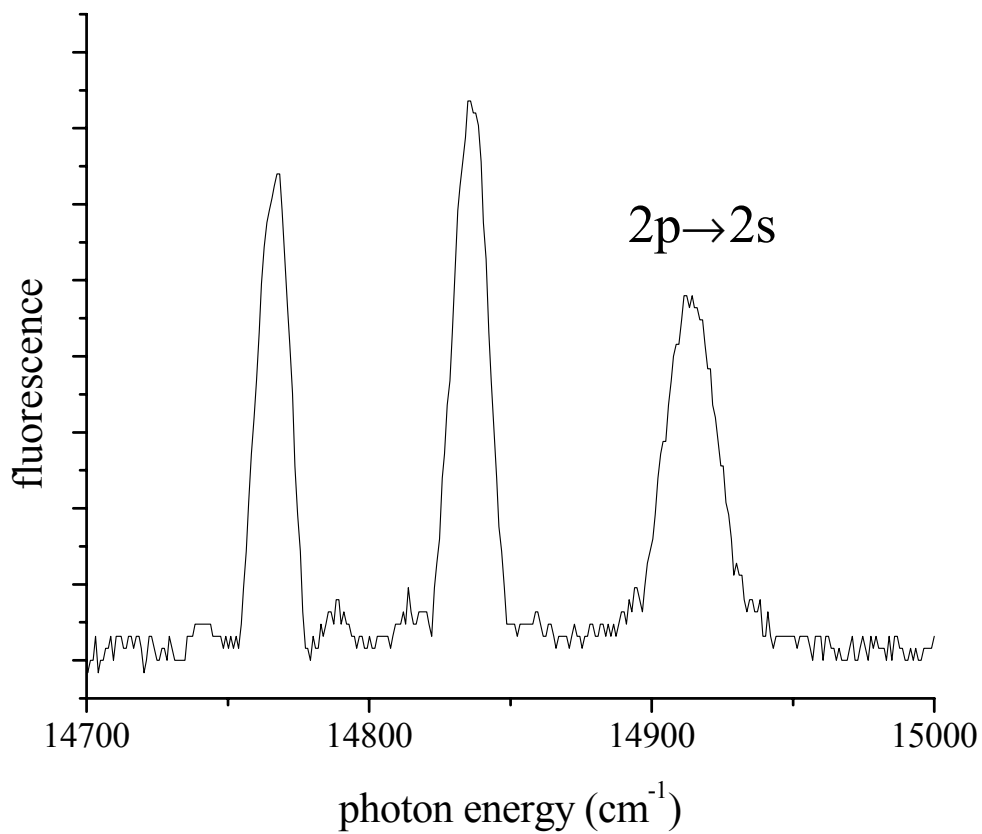


Figure 7.10: Fluorescence spectrum with excitation by 606.955 nm cw laser. The narrow peaks are molecular fluorescent lines with widths limited by the monochromator. The marked line corresponds to the  $2p \rightarrow 2s$  line of atomic lithium.

without any cw laser present. While optically chopping the pump pulse, it is seen that the timescales and spectral profiles of the transient peaks match remarkably well with those in the presence of the cw laser. This evidence supports the mechanism where the OPA excites the  $2p \leftarrow 2s$  transition from the atomic ground state followed by multiphoton ionization by the 800 nm pulse.

The proposed mechanism for the transient effect is a simple excitation of a fast decaying atomic state is supported by four primary pieces of evidence: the spectral profile of the ultrafast transient peak height coincides with the  $2p \rightarrow 2s$  transition in atomic lithium, the dramatic polarization dependence of the peak height, the presence of a wide bandwidth fluorescent line, and the presence of the effect without the cw laser. The fact that the effect is seen to depend on the cw laser (when optically chopping the cw laser) indicates that the cw laser somehow participates in the dynamical effect, but a mechanism is not proposed. Due to the evidence supporting the ultrafast effect being primarily atomic, further study on this system was preempted in favor of studies that are more directly molecular in nature [see chapters 1-6].

This chapter has summarized a series of experiments that address a transient signal in our pump-probe signals. Several series of experiments were performed in an attempt to infer the nature of the transient effect, but with little success since all of the molecular explanations are characterized by significant flaws. This argument was supported by several pieces of evidence including a dramatic pump-probe polarization dependence, the presence of an atomic

fluorescence line in an ostensibly molecular fluorescence spectrum, and the presence of the effect both with and without the cw laser.